1   **Anisotropy of magnetic susceptibility in natural olivine single crystals**

2

3   **Authors:**

4   Andrea R. Biedermann[1], Thomas Pettke[2], Eric Reusser[3], Ann M. Hirt[1,*]

5   [1] Institute of Geophysics, ETH Zurich, Sonneggstrasse 5, 8092 Zurich, Switzerland

6   [2] Institute of Geological Sciences, University of Bern, Baltzerstrasse 1-3, 3012 Bern,
7   Switzerland

8   [3] Institute of Geochemistry and Petrology, ETH Zurich, Clausiusstrasse 25, 8092 Zurich,
9   Switzerland

10

14 **Key points**

15 • the maximum susceptibility in fresh olivine with > 3wt.% FeO is parallel to *c*

16 • at RT the minimum susceptibility lies along *a* or *b* depending on the Fe content

17 • at 77 K the minimum susceptibility is parallel to the crystal's *b*-axis

18 **Keywords**

19 olivine

20 anisotropy of magnetic susceptibility

21 single crystal

22 magnetic properties

Abstract

Mantle flow dynamics can cause preferential alignment of olivine crystals that results in anisotropy of physical properties. To interpret anisotropy in mantle rocks, it is necessary to understand the anisotropy of olivine single crystals. We determined anisotropy of magnetic susceptibility (AMS) for natural olivine crystals. High-field AMS allows for the isolation of the anisotropy due to olivine alone. The orientations of the principal susceptibility axes are related to the olivine's crystallographic structure as soon as it contains > 3 wt.% FeO. The maximum susceptibility is parallel to the *c*-axis both at room temperature (RT) and at 77 K. The orientation of the minimum axis at RT depends on iron content; it is generally parallel to the *a*-axis in crystals with 3 – 5 wt.% FeO, and along *b* in samples with 6 – 10 wt.% FeO. The AMS ellipsoid is prolate and the standard deviatoric susceptibility, *k'*, is on the order of $8*10^{-10}$ m^3/kg for the samples with < 1wt.% FeO, and ranges from $3.1*10^{-9}$ m^3/kg to $5.7*10^{-9}$ m^3/kg for samples with 3-10 wt.% FeO. At 77 K, the minimum susceptibility is along *b*, independent of iron content. The shape of the AMS ellipsoid is prolate for samples with < 5 wt.% FeO, but can be prolate or oblate for higher iron content. The degree of anisotropy increases at 77 K with $p_{77}' = 7.1 \pm 0.5$. The results from this study will allow AMS fabrics to be used as a proxy for olivine texture in ultramafic rocks with high olivine content.

1 Introduction

Olivine is one of the most common minerals on Earth, constituting a large fraction of the Earth's upper mantle. Other terrestrial planets (Mercury, Venus or Mars) are also thought to have high concentration of olivine in their upper mantle. Olivine is also abundant in meteorites and contains inclusions of ferromagnetic minerals, which are capable of acquiring a remanent magnetization. Therefore, there has been interest in using olivine as a recorder of the extraterrestrial magnetic field (Hoffmann et al., 2011; Lappe et al., 2011; Rochette et al., 2009; Uehara and Nakamura, 2006). On Earth, the rheology of olivine determines flow dynamics in depths shallower than 410 km; thus, olivine properties influence mantle flow and plate tectonics. Plastic flow causes a preferred orientation of olivine crystals, which is responsible, for example, for seismic anisotropy in the upper mantle (e.g. Nicolas and Christensen, 1987; Silver, 1996). The crystallographic preferred orientation of olivine grains in peridotite bodies has been used to define flow dynamics in the upper mantle or detect lithospheric deformation (e.g. Hrouda et al., 2009). In addition, olivine texture can influence the location and orientation of deformation zones, because anisotropic viscosity causes a localization of shear stresses (Tommasi et al., 2009). These deformation zones can evolve into future plate boundaries.

Anisotropy of magnetic susceptibility (AMS) is commonly used as an indicator of the texture of a rock. The AMS of a whole rock consists of a superposition of diamagnetic and paramagnetic components which can be linked to silicate or carbonate minerals, and ferromagnetic components, which are associated with iron oxides, hydroxides or sulfides as inclusions or separate grains. Diamagnetic anisotropy is often negligible in rocks that contain iron-bearing minerals. Paramagnetic anisotropy, however, can be significant and arises principally from the distribution of iron ions in the crystal lattice. Consequently, magnetic

64   anisotropy arising from paramagnetic minerals can be used to determine the crystallographic

65   orientations of these minerals in a rock. To fully interpret the paramagnetic AMS, the single-

66   crystal properties of all the minerals in a rock must be known.

67   Only a few studies have been made on the magnetic anisotropy of natural olivine and

68   have yielded inconsistent results (Belley et al., 2009; Ferré et al., 2005a, b), and a summary is

69   given below. To resolve these inconsistencies in the literature, we conduct a thorough study of

70   the magnetic anisotropy of olivine, addressing the crystal chemistry, paramagnetic and

71   ferromagnetic contributions to the AMS and the relation of magnetic anisotropy to the

72   crystallographic lattice structure. We examine both low-field and high-field AMS in 35

73   olivine single crystals, focusing on natural samples, which are most relevant to mantle

74   deformation models. The main goal of this study is to define the single-crystal AMS of pure

75   olivine and to understand how it varies with chemical composition. Because magnetic

76   anisotropy is easily determined, allowing evaluation of a large number of samples, it can be

77   used as a first-order proxy for texture in mantle rocks, therefore mantle flow. Based on our

78   results, it will be possible to obtain insight into the rock texture from AMS measurements,

79   which are fast and easy to perform. This will have implications on fabric as well as

80   geodynamic studies. Because magnetic anisotropy can serve as a first-order proxy for texture

81   in mantle-derived rocks, it will also provide information on the relative degree of seismic

82   anisotropy.

2 Geophysical background

84   The olivine group includes the minerals olivine, forming a continuous solid solution

85   series between forsterite (Mg_2SiO_4) and fayalite (Fe_2SiO_4), tephroite (Mn_2SiO_4), knebelite

86   ((Mn,Fe)$_2SiO_4$), and monticellite ($Ca(Mg,Fe)SiO_4$) (Deer et al., 1997). Various members of

87   the forsterite-fayalite solid solution series are considered in this study, referred to as olivine.

88   Tephroite, knebelite and monticellite are subordinate on Earth. Mg-rich olivine dominates in

89   the Earth's upper mantle and is a common rock-forming mineral, especially in ultramafic

90   rocks (e.g. Deer et al., 1997). Olivine is an orthorhombic crystal with space group Pbnm. Its

91   structure consists of isolated $(SiO_4)^{4-}$ tetrahedra, which are linked mainly by Mg^{2+} or Fe^{2+} ions

92   in octahedral coordination. Other cations are almost exclusively divalent; if trivalent cations

93   are present, they occur in very small amounts. There are two types of distorted octahedral

94   sites, labeled M1 and M2, which have different symmetry: M1 sites represent centers of

95   symmetry, whereas M2 sites lie on mirror planes (Figure 1).
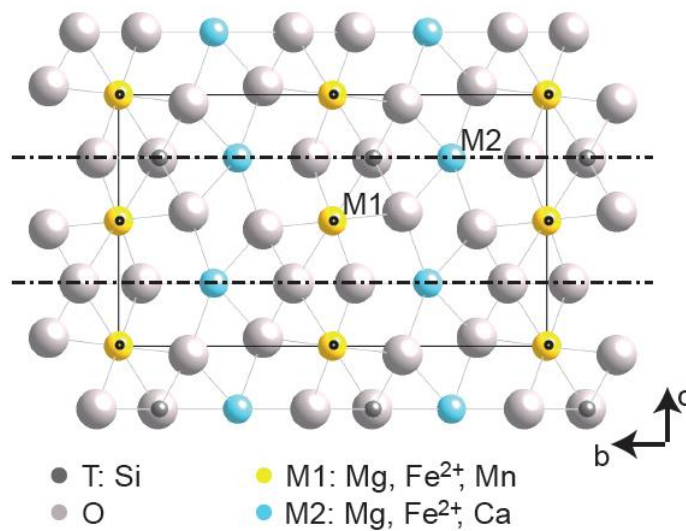
Figure 1: Olivine crystal structure, view along the a-axis. Oxygen and silicon atoms form tetrahedra, which are linked by magnesium or iron ions that can occupy either M1 or M2 sites. M1 sites represent inversion centers (o), whereas M2 sites lie on mirror planes (--).

102   Magnetic susceptibility is an intrinsic property of a material, relating the

103   magnetization induced by an applied magnetic field to the strength of the field. Susceptibility

104   anisotropy can be described by a second-order tensor. This tensor is symmetric and can be

105   represented by an ellipsoid whose principal axes ($k_1 \geq k_2 \geq k_3$) correspond to the eigenvalues

106   of the tensor. AMS can be described by a full tensor, whose elements are full directional

6

107 values of the susceptibility, or by a deviatoric tensor, whose elements are the differences in

108 susceptibility from the mean susceptibility. The magnetic susceptibility ellipsoid is generally

109 characterized by its degree of anisotropy and shape and the directions of the principal axes.

110 Because we use a method to isolate the paramagnetic anisotropy, which only gives the

111 deviatoric susceptibility, the degree of anisotropy is defined by the standard deviatoric

112 susceptibility, k' (Jelinek, 1984)

$$k' = \sqrt{\frac{(k_1 - k)^2 + (k_2 - k)^2 + (k_3 - k)^2}{3}}$$

113 where k is the mean susceptibility. The shape of the AMS ellipsoid is defined by U (Jelinek,

114 1981)

$$U = (2k_2 - k_1 - k_3)/(k_1 - k_3)$$

115 U is between 0 and +1 for an oblate ellipsoid, between 0 and -1 for a prolate ellipsoid

116 and close to 0 for a neutral ellipsoid.

117 The paramagnetic component of the susceptibility and its anisotropy vary with

118 temperature according to the Curie-Weiss law; the paramagnetic susceptibility becomes

119 enhanced with decreasing temperature and both the AMS degree and shape can vary as a

120 function of temperature.

121 AMS of a bulk rock is often used as a proxy for mineral fabric or deformation. For

122 example, Ferré et al. (2005b) found that the paramagnetic component of the high-field

123 anisotropy in mantle peridotite can be related to the lattice-preferred orientation of olivine. In

124 order to understand this relationship, however, it is essential to know the single-crystal

125 anisotropies of the minerals composing the rock. In the case of mantle peridotite this is Mg-

126 rich olivine.

127   Olivine often contains inclusions, such as iron-bearing oxides, sulfides or silicate melt.

128   Magnetite is a common ferrimagnetic mineral in mantle rocks. Developing at high

129   temperature in an olivine grain, magnetite often forms rods or lamellae in specific directions

130   in the olivine lattice. Magnetite in a rock can oxidize to hematite upon weathering and in

131   olivine hematite mainly occurs as diffusion rims along grain boundaries, thus indicating its

132   secondary origin (e.g. Deer et al., 1997). Iron sulphides, e.g. pyrrhotite, are also known to

133   occur as melt inclusions or grains in mantle rocks. In order to eliminate any contributions

134   from ferromagnetic (*s.l.*) inclusions to the magnetic anisotropy, the paramagnetic component,

135   which depends on the silicate structure, must be isolated. This paramagnetic fabric can be

136   related to the mineral fabric in the mantle. It is not possible to separate the paramagnetic

137   anisotropy when measuring low-field susceptibility. Because paramagnetism is linearly

138   related to the strength of the applied field, whereas ferrimagnetic minerals will be saturated in

139   fields < 600 mT, it is possible to separate the anisotropic component due to paramagnetic

140   minerals from that of saturated ferrimagnetic minerals (e.g. Hrouda, 1982; Owens and

141   Bamford, 1976). Thus, the paramagnetic anisotropy can be related to the olivine lattice.

142   The bulk susceptibility of olivine with various compositions was investigated first by

143   Nagata et al. (1957). They attributed the paramagnetic susceptibility of olivine to Fe^{2+} ions in

144   the crystal structure and found a linear relationship between molar susceptibility and fayalite

145   content x_{fa}:

146    $$\chi_{mol,olivine} = 2.2 * 10^{-2}x_{fa} \text{ to } 2.6 * 10^{-2}x_{fa} \text{ } emu/mol.$$

147   Later work by Hoye and O'Reilly (1972) and (Belley et al., 2009) in natural and synthetic

148   crystals or synthetic powders covered the complete compositional range between the forsterite

149   and fayalite end-members. Hoye and O'Reilly (1972) calculated olivine mass susceptibility

150   based on

$$\chi = \frac{2p_{eff}^2 \mu_B^2 xN}{3kM_\chi(T-\theta)}$$

151   where $p_{eff} = 5.2$ is the effective number of Bohr magnetons (μ_B) per iron atom, x the

152   fayalite mole fraction, N Avogadro's number, k Boltzmann's constant and M_χ the molar

153   weight of a crystal with fayalite content x, T is the measurement temperature and θ the

154   ordering temperature. They reported higher susceptibilities than predicted by Nagata's

155   formula. Belley et al. (2009) found $p_{eff} = 6.03$.

156   Several studies have examined the magnetic anisotropy in synthetic fayalite, Fe_2SiO_4

157   (Ballet et al., 1989; Cococcioni et al., 2003; Ehrenberg and Fuess, 1993; Müller et al., 1982)

158   and $(Fe,Mn)_2SiO_4$ (Ballet et al., 1987). Fayalite has been reported to undergo

159   antiferromagnetic ordering below 64.9 K, whereby the magnetic moments on the M2 sites are

160   parallel to the crystallographic b-axis, whereas those on M1 sites are canted (Ehrenberg and

161   Fuess, 1993). The canting angle decreases with temperature. The maximum susceptibility of

162   fayalite is parallel to the c-axis, independent of temperature. Below the Néel temperature, the

163   susceptibility anisotropy is clearly triaxial, with k_3 aligning with the b-axis. At room

164   temperature, however, the anisotropy is uniaxial with nearly equal susceptibilities parallel to

165   the crystallographic a- and b-axes of fayalite (Ballet et al., 1989; Ehrenberg and Fuess, 1993;

166   Müller et al., 1982). In its ground state, spins are coupled antiferromagnetically between

167   corner-sharing octahedra and ferromagnetically between edge-sharing octahedra (Cococcioni

168   et al., 2003; Müller et al., 1982). Ballet et al. (1987) concluded that the ionic anisotropy of

169   Fe^{2+} is responsible for the crystal anisotropy and that the easy direction of magnetization

170   depends on the relative distribution of Fe^{2+} on M1 and M2 sites. If Fe^{2+} is primarily located

171   on M1 sites, the easy magnetization direction is parallel to the crystallographic c-axis,

172   whereas it is parallel to b when Fe^{2+} is concentrated on M2 sites.

173   Belley et al. (2009) investigated the AMS of four olivine crystals with composition

174   close to forsterite and found that the maximum susceptibility was parallel to *a*, and the

175   minimum susceptibility parallel to *b*. They attributed the disagreement with the fayalite

176   studies to the different chemical composition. Ferré et al. (2005b) measured one crystal with

177   forsterite composition and found a maximum susceptibility along *c*, and minimum

178   susceptibility along *b*. The authors corrected this original finding to a maximum susceptibility

179   parallel to *a*, and minimum parallel to *c* (Ferré et al., 2005a).

180   **3 Methods**

181   **3.1 Sample description**

182   A collection of 35 natural olivine single crystals were investigated (Table 1). Samples

183   were borrowed from the Natural History Museum Basel (labeled NMB), the Mineral

184   Collection of ETH Zurich, Durham University, the Swiss Gemmological Institute or collected

185   during fieldwork. The samples are from different geological environment and cover the

186   compositional range from $x_{Mg} = 0.82$ to 0.99. Seven crystals (Ol16 – Ol22) are San Carlos

187   olivine, extracted from peridotite xenoliths, which are often used as reference crystals. Four

188   crystals were extracted from a peridotite xenolith in Cenozoic basalt from the Hannuoba area

189   in the North China craton (Ol9 – Ol12). These xenoliths contain coarse- to medium-grained

190   spinel lherzolite and are described by Chen et al. (2001) and Rudnick et al. (2004). The two

191   forsterite specimens (Fo1, Fo2) originate from a skarn in Burma. Samples Ol1, Ol14, Ol15,

192   Ol23 – Ol31, NMB45445 and NMB47213 are gem-quality crystals from the Sapat mafic-

193   ultramafic complex, Pakistan (Kane, 2004). There, the gem-olivine occurs in fluid-derived

194   veins in the dunite, that represents the arc mantle of the Kohistan arc (Bouilhol et al., 2009;

195   2012). A similar genetic type of olivine (NMB14203) is found on Zabargad Island, Egypt,

196   which is also known for its gem-quality olivine. Here, olivinite veins cut ultramafic bodies,

197 representing fertile upper mantle material, such as spinel and spinel-plagioclase lherzolite

198 (Kurat et al., 1993). Another sample (NMB28855) comes from Arizona, US; its exact

199 location, however, is not known. Samples Ol2 and Ol3 also come from unknown locations.

200 Four samples (Ol32-Ol35) were collected south of Oldoinyo Lengai, Tanzania. These crystals

201 are strongly weathered and exhibit a brown color typical for iddingsitation.

202 **3.2 Chemical composition**

203   In order to correlate magnetic properties of olivine with their chemistry, the *bulk*

204 sample chemical composition is required, because inclusions, whether they are

205 submicroscopic or microscopic, can affect magnetization parameters. Compositional data

206 were therefore acquired for most samples by laser-ablation inductively coupled plasma mass

207 spectrometry (LA-ICP-MS) at the Institute of Geological Sciences, University of Bern.

208 Details of instrumental setup and optimization strategies are reported elsewhere (Pettke et al.,

209 2012). LA-ICP-MS was preferred to conventionally employed electron probe microanalysis

210 (EPMA), because LA-ICP-MS allows analysis of a larger sample volume than that analyzed

211 by EPMA. In this way, the average composition of a large sample can be determined

212 accurately with fewer spot measurements than would be required for EPMA, while

213 maintaining analytical resolution to identify crystal-chemical zoning at the 100 μm scale. It

214 should be noted however, that analytical accuracy for major element composition is inferior

215 for LA-ICP-MS (1-2 % 2SD) relative to that typical of EPMA. A 120 μm wide beam was

216 used with LA-ICP-MS and at least four spots were measured per crystal to investigate

217 chemical homogeneity. Element concentration data were calculated assuming that the total of

218 major oxides is 100 wt.% and that iron is present exclusively as Fe^{2+}. Data processing was

219 performed using SILLS (Guillong et al., 2008).

220   Chemical analysis of the gemstone quality crystals Ol23-Ol31 was performed using

221   EPMA, because no destructive measurements were possible on these samples (cf. Bouilhol et

222   al., 2012, for ICP-MS analyses of samples from the Sapat complex). Each crystal was

223   wrapped in aluminum foil prior to measurement. A hole was cut into the foil above the best

224   natural surface of the crystal and a drop of silver served as conductor. The analyses were

225   made on a JEOL JXA-8200 electron microprobe at the Institute of Geochemistry and

226   Petrology, ETH Zurich. The instrument was operated at an accelerating voltage of 15 kV, a

227   beam current of 20 nA and with a focused beam. Synthetic forsterite and fayalite and

228   synthetic and natural oxides were used as standards. Several spots have been measured to

229   check for sample homogeneity. The data was φ-ρ-z corrected.

230   **3.3 Magnetic measurements**

231   Accurate crystallographic orientation of samples is mandatory for relating magnetic

232   anisotropy to crystal structure. The orientation of each single crystal was determined by Laue

233   X-ray diffraction measured at the Laboratory of Crystallography, ETH Zurich. The X-rays

234   were generated in a Mo-tube operated at 50 kV and 35 mA. The Laue photographs were

235   acquired in reflection mode with 4 minutes exposure time. Data analysis was performed using

236   the OrientExpress orientation software (Laugier and Filhol, 1983). With this method, crystals

237   could be oriented to an accuracy of ± 2 degrees. All magnetic measurements were made at the

238   Laboratory of Natural Magnetism, ETH Zurich.

239   **3.3.1 Acquisition of isothermal remanent magnetization (IRM) and hysteresis properties**

240   Acquisition of IRM was used to identify ferromagnetic inclusions in the olivine

241   crystals. For this purpose, the sample was magnetized with a pulse magnetizer (ASC

242   Scientific, IM-10-30) in a field of 2 T in a known direction. Then, the sample was

243   remagnetized in progressively higher fields in the opposite direction. After each applied field,

244   the magnetization was measured with a 2G Enterprises cryogenic magnetometer (Model 755).

245 The saturation remanent magnetization (SIRM) and remanent coercivity indicate the relative

246 concentration and type of ferromagnetic grains in the sample.

247 Hysteresis curves were measured on selected samples on a Princeton Measurements

248 Corporation MicroMag 3900 vibrating sample magnetometer (VSM) in fields up to 1 T to

249 further help identify the ferromagnetic minerals, based on their coercivity and saturation

250 magnetization. Magnetization curves were obtained using mixed increments of 10 mT

251 between 100 mT and 1000 mT, 1 mT between 20 mT and 100 mT and 0.5 mT for applied

252 fields lower than 20 mT. The slope of the high-field hysteresis curve was used as an

253 independent estimate of the paramagnetic susceptibility.

254 **3.3.2 Low-temperature magnetization curves**

255 Low-temperature magnetization curves were measured on two crystals on which

256 destructive measurements were allowed. Magnetization parallel to each of the

257 crystallographic axes was measured on a Quantum Design Magnetic Property Measurement

258 System (MPMS) at the Laboratory for Solid State Physics, ETH Zurich. The temperature-

259 dependence of the susceptibility was measured in fields of 1 T and 0.01 T and for a

260 temperature range between 300 K and 2 K. The cooling rate was 10 K/min and the

261 temperature was stabilized prior to each susceptibility measurement.

262 **3.3.3 Anisotropy of magnetic susceptibility**

263 Anisotropy of magnetic susceptibility was measured in low and high magnetic fields.

264 The sum of the diamagnetic, paramagnetic and ferromagnetic contributions of all mineral

265 grains in the sample is measured with both instruments. Low-field AMS was determined with

266 an AGICO MFK1-FA Kappabridge in a magnetic field of 200 A/m and with a frequency of

267 976 Hz. Weak samples were remeasured in 500 A/m fields. The susceptibility tensor was

268 calculated from 15 directional measurements. In order to increase data quality, the values for

269 ten measurements in each direction were stacked (Biedermann et al., 2013).

270   High-field AMS was measured on a torque magnetometer in six different fields

271 between 1.0 T and 1.5 T (Bergmüller et al., 1994). Measurements were obtained in three

272 mutually perpendicular planes, using a 30° measurement increment in each plane. The torque

273 magnetometer determines only the deviatoric susceptibility tensor. High-field measurements

274 were conducted both at room temperature and at 77 K. The fields, which were applied, are

275 large enough to saturate magnetite inclusions. When saturated, the ferromagnetic contribution

276 to the torque signal is independent of any increase in the field, whereas the paramagnetic

277 contribution increases in proportion to the square of the field. This allows for separation of the

278 diamagnetic, paramagnetic and ferrimagnetic contributions to the high-field AMS (Martín-

279 Hernández and Hirt, 2001, 2004; Schmidt et al., 2007).

4. Results

4.1 Chemical composition

282   The olivine sample suite covers the compositional range from Fo90 to Fo99 for the

283 fresh samples and Fo80 for the strongly weathered olivines (Table 1, and Table A – Online

284 Supplementary). Low spot-to-spot variability of most elements indicates that cations are

285 homogeneously distributed within most crystals. There are several exceptions, such as for

286 NMB45445, which exhibits macroscopically visible dark needle-shaped inclusions.

287 According to Bouilhol et al. (2012), needles of Mg-Fe borates are characteristic for Sapat

288 olivine. Sample Ol14 comprises spherical black inclusions that may correspond to magnetite.

289 Additionally, Ol2 and NMB28855 contain melt inclusions characterized by elevated bulk

290 contents of Fe and high concentrations of rare earth elements. In the fresh samples, the Ni

291 content varies between 1900 and 3200 µg/g. Other cations with large magnetic moments, such

as Cr or Mn, are only present in very small amounts (< 1 wt.% MnO; < 400 µg/g Cr). The weathered samples from Tanzania have different compositions, with higher iron contents, and larger amounts of other elements such as Ti, Mn, Ca, Na, K, Zn, Sr and Zr, compared to fresh olivine. Their Ni content varies between 1000 and 1100 µg/g and Cr is ca. 60 µg/g.

4.2 IRM acquisition and hysteresis

The acquisition of IRM was measured on selected crystals from the different localities (Figure 2). All samples have a remanent coercivity < 50 mT, and samples NMB45445, Ol14 and Ol31 have a coercivity value < 20 mT. Samples NMB45445 and NMB47213, Ol14 and Ol15 saturate in fields below 200 mT, while the remaining crystals are saturated by 300 mT. NMB45445, Ol14, Ol34 and Ol35 have the strongest saturation magnetizations indicating the highest concentrations of ferromagnetic inclusions (Table 2). It should be noted that saturation is reached well below 1 T, which allows for a reliable separation of paramagnetic and ferromagnetic contributions using high-field AMS.
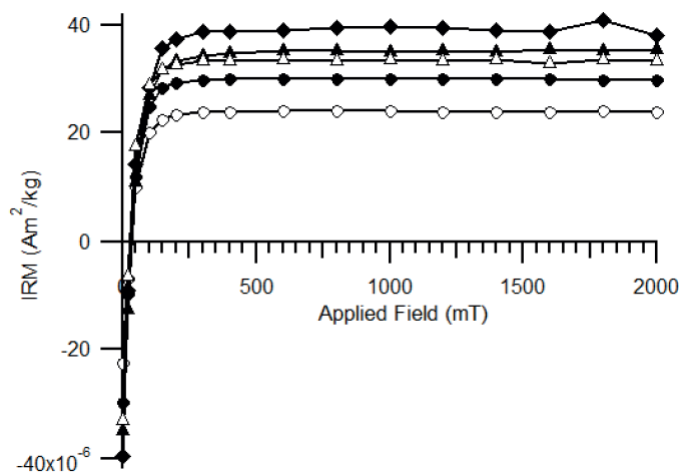
Figure 2: Representative IRM acquisition curves show low coercivities and saturation fields for the ferromagnetic inclusions.

309   Hysteresis was measured on the samples small enough to fit in-between the poles of

310 the vibrating sample magnetometer. Many samples showed a positive linear relationship

311 between field and magnetization, which indicates the presence of only a paramagnetic

312 component. Those samples with a ferromagnetic (*s.l.*) contribution showed low coercivities

313 and were magnetically saturated by 300 mT. Because the cryogenic magnetometer is more

314 sensitive in detecting remanent magnetization than the VSM, magnetite was identified in Ol2

315 and Ol3 from IRM acquisition, whereas the hysteresis curves show a pure paramagnetic

316 component.

317 **4.3 Magnetic susceptibility and anisotropy**

318 **4.3.1 Low-temperature susceptibility**

319   Low-temperature susceptibility was determined for Ol14 and Ol15. The measurements

320 show that the increase in directional susceptibility with decreasing temperature is anisotropic.

321 For temperatures larger than ca. 100 K, the susceptibility can be approximated by a Curie-

322 Weiss law along all three crystallographic axes:

$$\chi_{obs} = \frac{M}{H} = \mu_0 \frac{C}{T - \theta} + \chi_0$$

323 where χ_{obs} is the molar susceptibility, M the measured magnetization in the applied field H,

324 μ_0 the permeability of free space, C the Curie constant and χ_0 a temperature-independent

325 background, such as diamagnetic or van Vleck paramagnetic susceptibility. The Curie

326 constant is defined as:

$$C = \frac{\mu_B{}^2 g^2 S(S + 1) N}{3 k_b}$$

327 where μ_B is the Bohr magneton, g is Landé's g-factor, S is the spin number, N is the number

328 of magnetic ions, and k_b is Boltzmann's constant. Ferrous iron possesses a spin S = 2. The

329 material constants g and θ depend on the crystallographic direction as shown in Table 3.

330   Local magnetic ordering sets in below approximately 100 K when the field is parallel

331   to b, resulting in a smaller increase in the susceptibility than predicted by the Curie-Weiss

332   Law when the temperature is decreased further. When the field is applied along the

333   crystallographic a-axis, the measured susceptibility is stronger than predicted below 60 K for

334   Ol15 or 90 K for Ol14. Only a minor deviation towards higher susceptibility compared to

335   Curie-Weiss behavior can be seen in Ol15 for T < 10 K when the field is parallel to the c-axis.

336   In relation to the anisotropy measured, the susceptibility along the a- and b-axes is very

337   similar ($1.84*10^{-8}$ m^3/mol and $1.80*10^{-8}$ m^3/mol for Ol14, and $2.47*10^{-8}$ m^3/mol and $2.38*10^{-}$

338   ^{8} m^3/mol for Ol15) at room temperature. At 77 K the susceptibility parallel to the b-axis is

339   affected by the onset of local magnetic order and smaller than the susceptibility parallel to a

340   (Figure 3).
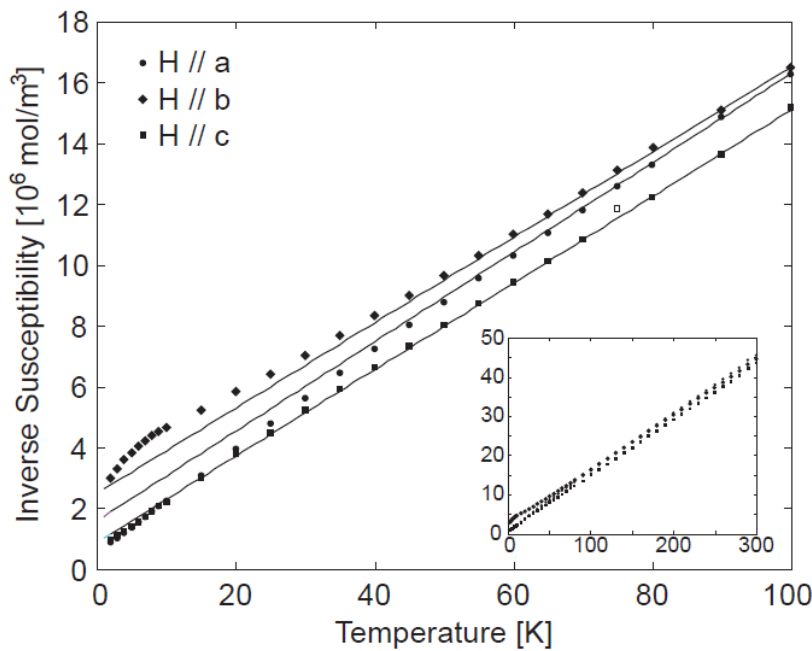
341

342   *Figure 3: Inverse molar susceptibility along the three crystallographic axes plotted as a function of*
343   *temperature. Symbols represent measured data and lines the modelled paramagnetic susceptibility.*
344

4.3.2 Low-field AMS

Most crystals in the Fo90 – Fo96 range have mean susceptibility on the order of 1.5* 10^{-7} m^3/kg; there is a good agreement with the high-field susceptibility χ_{hf}, on crystals where this was determined. The mean susceptibilities of e.g. NMB45445 and Ol14 are five to 20 times larger than those of the other fresh crystals, which is due to ferrimagnetic inclusions. The weathered crystals have higher mean susceptibilities and show a larger variation. The forsterite crystals Fo1 and Fo2 have very weak susceptibilities and appear diamagnetic when measured on the MFK1 susceptibility bridge but paramagnetic on the VSM, which might be explained by incomplete subtraction of the holder signal, i.e. the glue used to fix the sample within the plastic cylinder was not corrected for in the MFK1 measurement. It cannot be ruled out that the glue also influenced the low-field AMS of forsterite, however, it is not expected that the effect is large given the relative amounts of crystal and glue. All other crystals display mean susceptibilities that are at least an order of magnitude higher than that of forsterite and the effect of the glue is negligible. The low-field AMS of each crystal was measured 10 times, and averaged principal directions are shown for each crystal in Figure 4. The anisotropy is significant for all crystals except Ol11. The maximum susceptibility groups around the crystallographic *c*-axis, whereas the intermediate and minimum susceptibilities are distributed in the *a-b*-plane. Nearly all crystals have inherent anisotropies between 3 % and 10 % (*P* = 1.03 – 1.10), except for samples with ferromagnetic contributions, which have a higher degree of anisotropy. This is best illustrated in samples that showed a high saturation remanence, e.g. NMB45445 and Ol14 with P = 3.03 and 2.54, respectively. The large P-values of the two forsterite crystals are due to their weak susceptibility (cf. Hrouda, 2004; Biedermann et al., 2013). Most samples display a prolate shape of the low-field AMS ellipsoid (Table B – Online Supplementary).

369
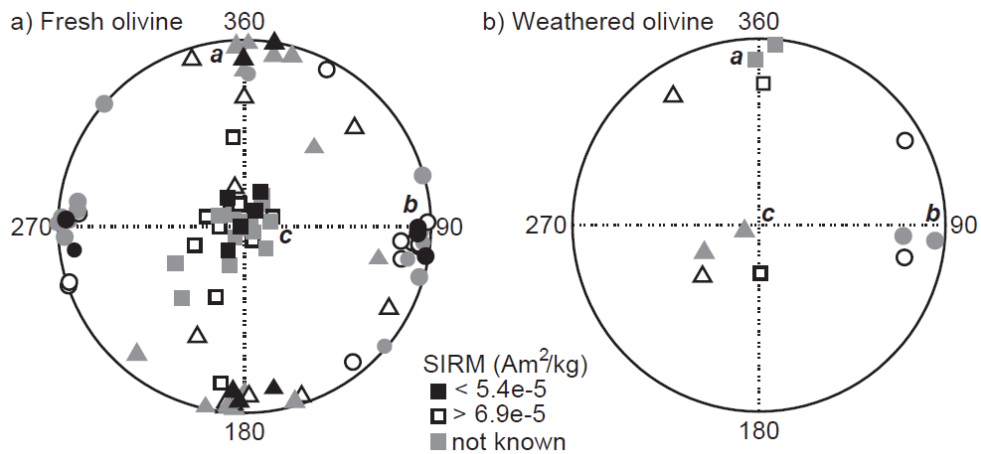
Figure 4: Lower-hemisphere, equal area stereoplots of the low-field AMS of fresh (a) and weathered (b) olivine crystals. Letters indicate crystallographic directions. k_1 are represented by squares, k_2 by triangles and k_3 by circles for this and subsequent figures.

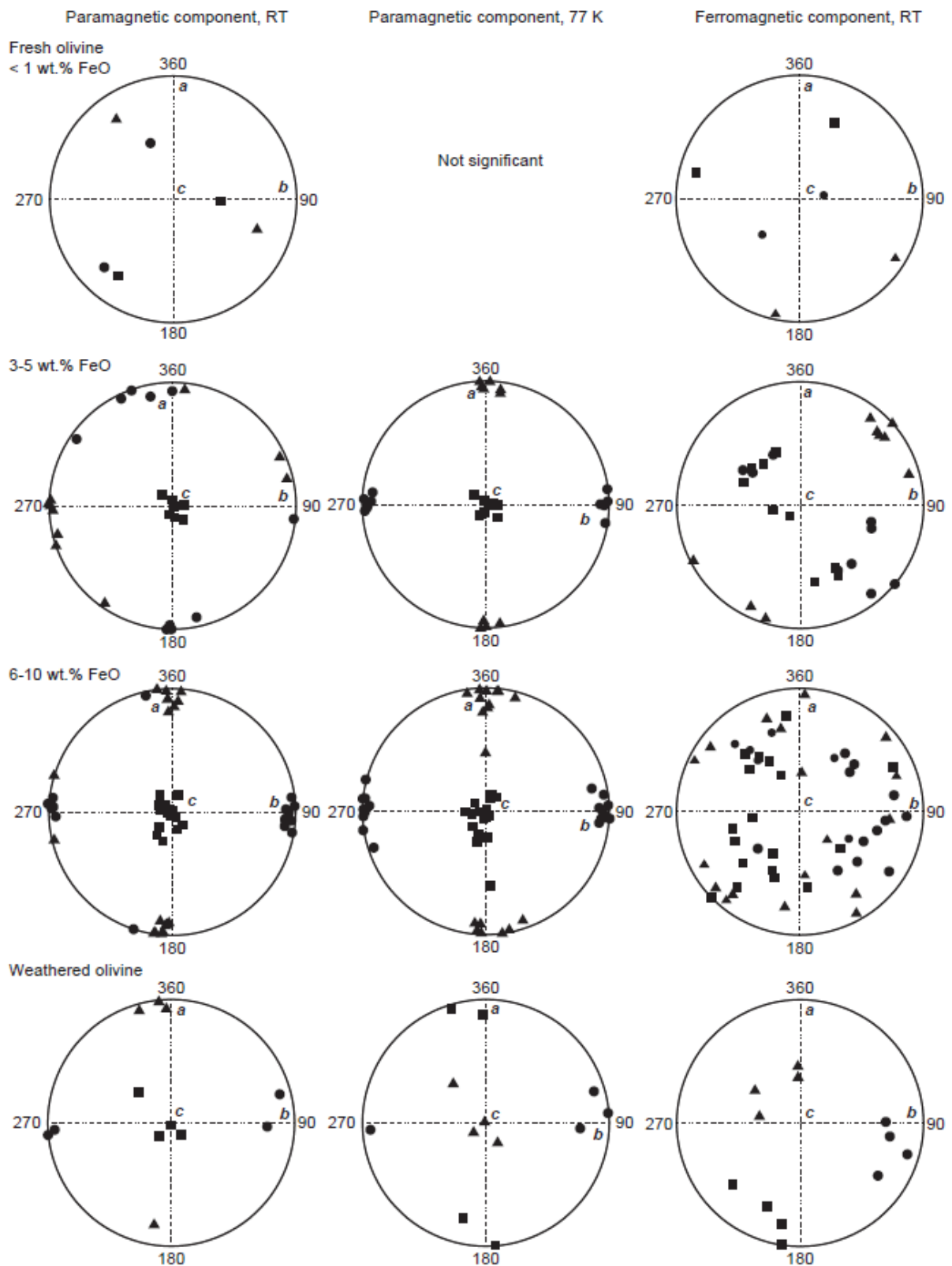### 4.3.3 High-field AMS

Torque measurements in high fields, unlike the low-field measurements, allow for separation of paramagnetic and ferrimagnetic contributions to the AMS. The torque for the forsterite crystals is weak but significant at room temperature. At low temperature, however, the noise level is higher and dominates the torque signal. The principal susceptibilities show different directions for both crystals at room temperature and neither is parallel to the crystallographic axes. AMS directions are not well defined for these crystals because the torque response is at the sensitivity level of the torquemeter. This could be due to a superposition of diamagnetic and paramagnetic fabrics, as indicated by the decrease in anisotropy at low temperature. A separation of these two components was not possible.

For most of the crystals with > 3 wt.% FeO, the paramagnetic component is dominant, and responsible for ca. 90 % of the anisotropy (Table C – Online Supplementary). A typical example of the torque signal is shown in Figure A – Online Supplementary. The anisotropy of one crystal, Ol11, was not significantly above the noise level. For all other samples, the principal paramagnetic susceptibilities are clearly related to crystallographic axes of the

19

389　olivine crystals. The k_1 axes are aligned along c in all fresh olivine crystals. Of these, 10

390　crystals have 3-5 wt.% FeO and 19 samples (18 of which have significant anisotropy) contain

391　6-10 wt.% FeO. For most crystals of the latter group, k_2 is along the a- axis and k_3 is along the

392　b-axis at room temperature. For the crystals whose FeO-content is $3 - 5$ wt.%, k_3 is

393　dominantly along the crystallographic a-axis. The degree of anisotropy, k', varies from

394　$3.1*10^{-9}$ m^3/kg to $5.7*10^{-9}$ m^3/kg and the U-parameter is prolate for all samples except one

395　and ranges from -0.99 to +0.14. The weathered samples have their maximum paramagnetic

396　susceptibility parallel to the crystallographic c-axis, and the minimum susceptibility parallel

397　to the b-axis, similar to the other crystals with higher iron content. However, they have more

398　oblate ellipsoid shapes, with U ranging from 0.02 to 0.23.

399　　　The paramagnetic anisotropy becomes more dominant at 77 K. The orientation of the

400　k_1 axes does not change significantly in the fresh samples, but the k_2 axes are all oriented

401　about the a-axis of their respective crystals, and the k_3 axes are grouped around the b

402　crystallographic axes (Figure 5). The weathered olivine shows a different behavior at 77K;

403　while the minimum susceptibility remains parallel to the b-axis, the maximum is now parallel

404　to the a-axis. The shape of the AMS ellipsoids are shifted towards the oblate field at low

405　temperature (Figure 6). At 77 K, the fresh olivine exhibits U-values between -0.55 and +0.35

406　and the weathered olivine has U between +0.55 and +0.67. The degree of the paramagnetic

407　anisotropy increases with decreasing temperature. This increase can be quantified by p'_{77},

408　defined as $p'_{77} = k'_{77K}/k'_{298K}$, which is not significantly different from p_{77} defined by

409　Schmidt et al. (2007). The degree of the paramagnetic contribution to the high-field AMS

410　increases at 77 K by an average of 7.1 ± 0.5 with respect to room temperature for fresh olivine

411　and 8.0 ± 0.3 for weathered crystals.

412

Figure 5: Lower-hemisphere, equal area stereoplots of the paramagnetic and ferromagnetic principal
directions of the high-field AMS for fresh samples with different iron contents and for weathered
samples.

417
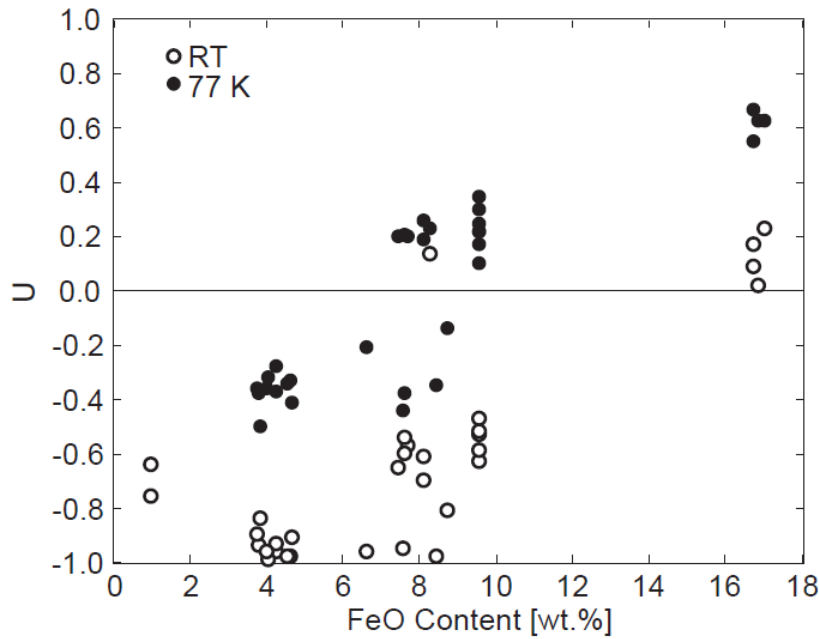
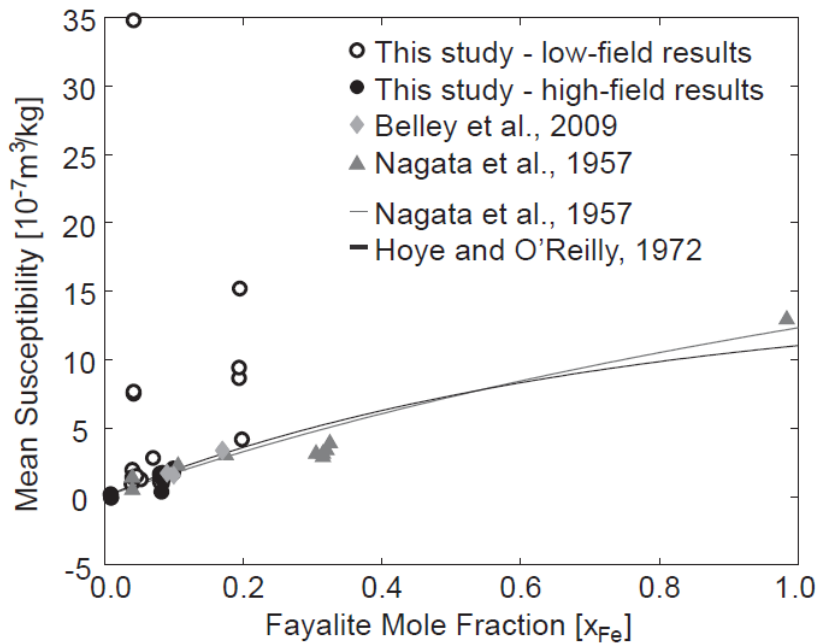*Figure 6: AMS shape U as a function of iron content.*

418
419

420   The ferromagnetic component of the anisotropy is weak and usually contributes less

421   than 10 % to the torque signal. Even though the contribution is not significant for most

422   samples, the principal directions of this component are surprisingly consistent, in particular

423   for the crystals with 3-5 wt.% FeO, which are mainly from the Sapat Complex, Pakistan. The

424   maximum susceptibility of the ferromagnetic component is tilted 45° with respect to the

425   crystallographic c-axis of the olivine (Figure 5). The shape parameter U covers the entire

426   range from -0.83 to 0.87 and the anisotropy degree of the ferromagnetic AMS varies between

427    $1.3*10^{-10}$ m^3/kg and $2.8*10^{-8}$ m^3/kg (Table C – Online Supplementary).

5. Discussion

428

429   The mean magnetic susceptibility shows a general increase with iron content (Figure

430   7). Exceptions to this general trend are samples, whose susceptibilities are mainly due to

431   magnetite inclusions, e.g. Ol14 and NMB45445 and the weathered crystals. These crystals

432   displayed SIRM $> 7.1*10^{-4}$ Am^2/kg. Our data agree with the relationship of susceptibility and

433   fayalite content of both Nagata et al. (1957) and Hoye and O'Reilly (1972), within the limited

434   compositional range.

435

436   *Figure 7: Mean susceptibility as a function of iron content for this and other studies.*
437

438   At T $<$ 100 K, the susceptibility parallel to the crystallographic *b*-axis is lower than

439   expected based on the Curie-Weiss law. This can be attributed to the onset of local

440   antiferromagnetic interactions, which agrees with the occurrence of antiferromagnetic

441   ordering in fayalite as described by Ballet et al. (1989). The susceptibility along the *c*-axis

442   continues to follow the Curie-Weiss law down to 10 K in Ol15. Similarly, the susceptibility

443   along the *c*-axis in fayalite corresponds to a Curie-Weiss behavior below the Néel temperature

444   (Ballet et al., 1989). It appears that local ferromagnetic ordering may occur along the *a*-axis

445   due to canting of the spins, which could result from dipolar interaction, anisotropic exchange

446   coupling or a weak single ion anisotropy (Ballet et al., 1989; Ehrenberg and Fuess, 1993;

447   Müller et al., 1982). Overall, however, the antiferromagnetic interactions dominate. We found

448   Curie temperatures of -11 K, - 18 K and between -4 and -6 K for a magnetic field applied

449 parallel to the crystallographic *a*-, *b*- and *c*-axes respectively. Hoye and O'Reilly (1972)

450 provided a formula to calculate the Curie temperature, $\theta = -87x$, where *x* is the fayalite

451 mole fraction. In our samples, $x = 0.076$, which leads to $\theta = -6.6\,K$. This lies within the

452 range of directionally dependent temperatures found in our samples.The low-field anisotropy

453 has been shown to be influenced by ferromagnetic inclusions in the crystal. The principal

454 directions of low-field susceptibility lie close to the paramagnetic principal susceptibilities of

455 their respective crystals as long as the SIRM is not larger than $5.4*10^{-5}$ Am^2/kg. Mean

456 susceptibility on the other hand is less affected by the ferromagnetic inclusions until their

457 concentration increases by a factor of 10. Thus, the low-field magnetic anisotropy can be

458 affected by ferromagnetic inclusions in a crystal, where this may not be obvious from the

459 mean susceptibility values. Most samples with SIRM $> 6.9*10^{-5}$ Am^2/kg display an AMS

460 ellipsoid that is tilted with respect to the pure paramagnetic ellipsoid. Samples with SIRM $>$

461 10^{-4} Am^2/kg have higher *P*-values than samples that showed purely paramagnetic behavior

462 from their magnetization curves. The saturation remanence of many samples that acquired an

463 IRM indicates that the concentration of magnetite is very low, and does not have a significant

464 contribution to the mean susceptibility. These samples display no relationship between the

465 degree of anisotropy, expressed either as *P* or *k'*, with iron content (Figure B – Online

466 Supplementary). The higher *P*-values of the forsterites can be attributed to the low value of

467 mean susceptibility (Biedermann et al., 2013; Hrouda, 2004).

468   The paramagnetic component of the high-field AMS is related to the silicate lattice,

469 whereas the ferromagnetic component can be attributed to iron oxide inclusions. Olivine has

470 an orthorhombic crystal structure. According to Neumann's principle (Neumann, 1885), any

471 physical property of a crystal must include all symmetry elements of its point group. In the

24

472 case of an orthorhombic crystal, the principal axes of any second-order tensor property must

473 be parallel to the crystallographic axes.

474   A significant magnetic anisotropy was only found in the two forsterite crystals when

475 measured at room temperature in high fields, and their principal AMS directions are variable.

476 This could be explained by varying contributions of paramagnetic and diamagnetic effects.

477 The samples become less anisotropic at low temperature, i.e. enhancement of the temperature-

478 dependent paramagnetic contribution is more isotropic. This suggests that the observed

479 anisotropy at room temperature arises from a combination of paramagnetic and diamagnetic

480 contributions or van Vleck paramagnetism.

481   All crystals containing more than 3 wt.% FeO show a clear alignment of the principal

482 susceptibilities with the crystallographic axes. The grouping of paramagnetic principal

483 susceptibilities is better at low temperature, where the paramagnetic anisotropy is enhanced.

484 At low temperature, the minimum susceptibility is parallel to *b,* whereas it can be parallel to *a*

485 or *b* at room temperature, depending on the iron content. Fresh olivine crystals containing > 6

486 wt.% FeO show a similar relationship in the orientation of the principal axes of paramagnetic

487 anisotropy compared to published experimental and theoretical studies on fayalite − their

488 maximum susceptibility is parallel to the crystallographic c-axis, and the minimum

489 susceptibility parallel to the b-axis (Ballet et al., 1989; Ehrenberg and Fuess, 1993). Thus,

490 their AMS can be explained by the large magnetic moment of iron, which dominates the

491 magnetic signal. Several studies have shown that for solid solutions in the olivine group, iron

492 atoms show a small preference for the M1 sites over the M2 sites (Deer et al., 1997 and

493 references therein). The enrichment of iron in M1 is variable and shows no correlation to

494 bulk composition. The preference of iron for M1 sites, together with the fact that Fe^{2+} on M1

495 sites results in an easy magnetization direction parallel to the *c*-axis (Ballet et al., 1987),

496 explains why the k_1 principal axes of the fresh crystals are parallel to *c*. In samples with $3 - 5$

497 wt.% FeO, the intermediate and minimum susceptibilities can be interchanged at room

498 temperature. The weathered crystals with FeO ~17 wt.% have their minimum susceptibility

499 parallel to *b* at both temperatures, but the maximum susceptibility switches from *c* to *a* at 77

500 K. The change in AMS principal directions between the fresh and weathered olivine crystals

501 can be attributed to the chemical alteration of olivine to iddingsite, which introduces

502 hydroxyls into the structure. This will affect the interatomic distances or crystal fields, which

503 will in turn influence the magnetic anisotropy.

504   The shape of the AMS is prolate for the fresh crystals at room temperature and more

505 neutral at 77 K. Müller et al. (1982) measured the temperature dependence of susceptibility in

506 fayalite between 4.2 K and 120 K and showed that the susceptibility is different along all

507 three axes at 4.2 K and 35 K, but that the susceptibilities along *a* and *b* are the same at 120 K.

508 A similar behavior is presented here for Mg-rich olivine – the susceptibilities parallel to the *a*-

509 and *b*-axes are nearly equal at room temperature, but differ at 77 K due to the onset of

510 magnetic ordering below ~100 K. The degree of anisotropy of the paramagnetic AMS

511 increases with iron content, although there is an additional variability in the data (Figure 8).

512 Further, the shape of the AMS ellipsoid is more prolate for samples with < 5 wt.% FeO than

513 for those with > 6 wt.% FeO, and the weathered samples all plot in the oblate field.

514   A ferromagnetic contribution to the susceptibility and its anisotropy was detected in

515 part of our samples, related to a low-coercivity phase such as magnetite. Although the

516 contribution of the ferromagnetic component of the AMS is weak, its directions are

517 consistent, with the maximum principal susceptibility tilted at 45° to the c-axis of the host

518 olivine. Several studies have shown that nucleation and growth of inclusions in olivine is

519 controlled crystallographically; e.g. Fe-Ni globules in chondritic olivine grows such that the

520 (110) axis of the metal is parallel to (100) of olivine (Lappe et al., 2011; Leroux et al., 2003).

521 We suggest tentatively that similar relationships may hold for magnetite in olivine. Further

522 work is needed, however, to investigate the directional relationship of magnetite inclusions in

523 terrestrial olivine.
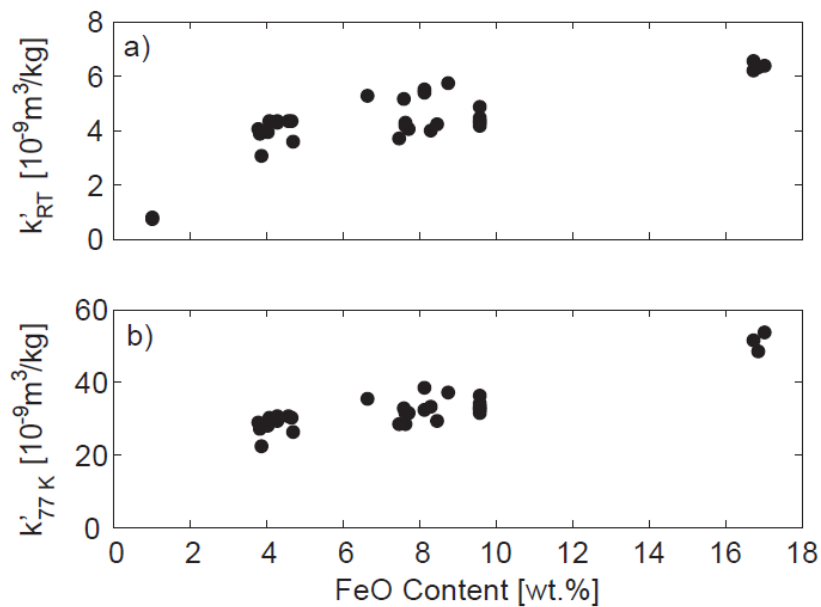
524

525 *Figure 8: High-field anisotropy degree, k', plotted as a function of Fe-content at room temperature (a)*
526 *and 77 K (b).*
527

528 Due to the well-defined magnetic anisotropy which is related to the crystallographic

529 lattice of olivine, AMS is a proxy for rock texture in olivine-dominated rocks. Olivine AMS

530 can be used to investigate deformation or flow patterns in the upper mantle. (Hrouda et al.,

531 2009) provides an example of how the AMS-derived fabric can give insight into processes of

532 emplacement of an ultramafic body. Furthermore, magnetic anisotropy may be used to infer

533 seismic anisotropy in the upper mantle.

534 If the orientation distribution function of crystals in an olivine-rich rock is known,

535 results for individual single crystals can be used to compute the magnetic anisotropy of the

536   bulk rock. This can be done for (1) the paramagnetic component, given that ferromagnetic

537   inclusions are absent or display random orientation, which would carry no anisotropy, and (2)

538   for the ferromagnetic component if ferromagnetic inclusions are consistently oriented with

539   respect to olivine. This is the case for several crystals used in this study that have a

540   ferromagnetic anisotropy. The ferromagnetic fabric will be dependent on when the

541   ferromagnetic minerals formed. For example, exsolution products are structurally oriented

542   with respect to the host olivine, whereas minerals formed during alteration processes do not

543   necessarily display a preferred orientation (Deer et al., 1997; Haggerty and Baker, 1967;

544   Xueixiang et al., 2009). With new satellite data coverage from the up-coming SWARM

545   mission (e.g. Friis-Christensen et al., 2006), detailed information on crustal magnetic

546   anomalies will become available. Our data are central to the proper interpretation of magnetic

547   anomalies over ultramafic bodies, because the paramagnetic and ferromagnetic anisotropies

548   cause a tilt in the magnetization with respect to the magnetic field. In other words, rock

549   texture can deflect magnetization that will thus not be parallel to the ambient magnetic field,

550   but can be tilted towards the magnetic lineation. This anisotropy may have to be taken into

551   consideration when modeling observed magnetic anomalies.

6. Conclusions

553   The magnetic signal of olivine is dominated by iron. Mg^{2+}, Si^{4+} and O^{2-} are all

554   diamagnetic whereas Fe^{2+} is paramagnetic and possesses a strong magnetic moment. Pure

555   forsterite should have a negative mean susceptibility and exhibit a purely diamagnetic

556   anisotropy. The forsterite crystals (Fo1, Fo2) contain 1 wt.% FeO, which is sufficient to cause

557   a positive susceptibility. The AMS of the forsterite crystals is thus a superposition of

558   diamagnetic and paramagnetic contributions, which explains why the principal susceptibilities

559   are not parallel to the crystallographic axes.

560   Our study has demonstrated that the principal axes of paramagnetic susceptibility can

561   be directly linked to certain crystallographic axes as soon as > 3 wt.% FeO are present in an

562   olivine crystal. If the iron content is between 6 and 10 wt.% FeO in fresh crystals, the

563   maximum and minimum susceptibilities are parallel to the *c*- and *b*-axes, respectively. For

564   crystals with iron contents between 3 and 5 wt.%, the minimum susceptibility is mostly

565   parallel to the *a*-axis, while the maximum susceptibility remains along the *c*-axis. This is due

566   to the ionic anisotropy of iron in the M1 sites, its preferred location. At room temperature, the

567   AMS ellipsoid is highly prolate, especially for samples with iron contents < 5 wt.% FeO.

568   Samples with 6 to 10 wt.% FeO display a prolate anisotropy ellipsoid, but with a larger

569   difference between k_2 and k_3 than samples with < 5 wt.% FeO. At 77 K, the AMS is triaxial

570   for all samples. These results do not agree with the results in Belley et al. (2009) or Ferré et

571   al. (2005a). They do agree, however with Ferré at al. (2005b) and with AMS results for

572   fayalite (Ballet et al., 1989; Cococcioni et al, 2003; Ehrenberg and Fuess, 1993; Müller et al.,

573   1982). The degree of high-field anisotropy increases by a factor (p'_{77}) of 7.1 ± 0.5 at 77 K

574   compared to room temperature. The different behavior displayed by the weathered crystals

575   highlights how differences in mineral composition can affect the AMS. Our findings have

576   great potential for using AMS as a proxy for mantle deformation. They also have implications

577   for modeling magnetic anomalies observed over deformed ultramafic rock domains.

References

Ballet, O., Fuess, H., Fritzsche, T., 1987. Magnetic Structure and Cation Distribution in (Fe,Mn)$_2$SiO$_4$ (Olivine) by Neutron Diffraction. Physics and Chemistry of Minerals 15, 54-58.

Ballet, O., Fuess, H., Wacker, K., Untersteller, E., Treutmann, W., Hellner, E., Hosoya, S., 1989. Magnetisation measurements of the synthetic olivine single crystals A$_2$SiO$_4$ with A = Mn, Fe or Co. Journal of Physics-Condensed Matter 1, 4955-4970.

Belley, F., Ferré, E.C., Martín-Hernández, F., Jackson, M.J., Dyar, M.D., Catlos, E.J., 2009. The magnetic properties of natural and synthetic (Fe$_x$, Mg$_{1-x}$)$_2$ SiO$_4$ olivines. Earth and Planetary Science Letters 284, 516-526, doi: 10.1016/j.epsl.2009.05.016

Bergmüller, F., Bärlocher, C., Geyer, B., Grieder, M., Heller, F., Zweifel, P., 1994. A torque magnetometer for measurements of the high-field anisotropy of rocks and crystals. Measurement Science and Technology 5, 1466-1470.

Biedermann, A.R., Lowrie, W., Hirt, A.M., 2013. A method for improving the measurement of low-field magnetic susceptibility anisotropy in weak samples. Journal of Applied Geophysics 88, 122-130, doi: 10.1016/j.jappgeo.2012.10.008.

Bouilhol, P., Burg, J.-P., Bodinier, J.-L., Schmidt, M.W., Dawood, H., Hussain, S., 2009. Magma and fluid percolation in arc to forearc mantle: Evidence from Sapat (Kohistan, Northern Pakistan). Lithos 107, 17-37, doi: 10.1016/j.lithos.2008.07.004.

Bouilhol, P., Burg, J.P., Bodinier, J.L., Schmidt, M.W., Bernasconi, S.M., Dawood, H., 2012. Gem olivine and calcite mineralization precipitated from subduction-derived fluids in the Kohistan Arc-Mantle (Pakistan). The Canadian Mineralogist 50, 1291-1304, doi: 10.3749/canmin.50.5.1291.

Chen, S.H., O'Reilly, S.Y., Zhou, X.H., Griffin, W.L., Zhang, G.H., Sun, M., Feng, J.L., Zhang, M., 2001. Thermal and petrological structure of the lithosphere beneath Hannuoba, Sino-Korean Craton, China: evidence from xenoliths. Lithos 56, 267-301.

Cococcioni, M., Dal Corso, A., de Gironcoli, S., 2003. Structural, electronic, and magnetic properties of Fe$_2$SiO$_4$ fayalite: Comparison of LDA and GGA results. Physical Review B 67, 094106, doi: 10.1103/PhysRevB.67.094106.

Deer, W.A., Howie, R.A., Zussman, J., 1997. Rock-Forming Minerals, Volume 1A, Orthosilicates, 2nd ed. The Geological Society, London, UK.

Ehrenberg, H., Fuess, H., 1993. Analytical interpretation and simulation of the static magnetic properties of synthetic alpha-Fe$_2$SiO$_4$. Journal of Physics-Condensed Matter 5, 3663-3672.

Ferré, E.C., Tikoff, B., Jackson, M., 2005a. Corrigendum to "The magnetic anisotropy of mantle peridotites: Example from the Twin Sisters dunite, Washington"

621   [Tectonophysics 398 (2005) 141–166]. Tectonophysics 405, 233, doi:
622   10.1016/j.tecto.2005.06.001.

623 Ferré, E.C., Tikoff, B., Jackson, M., 2005b. The magnetic anisotropy of mantle peridotites:
624   Example from the Twin Sisters dunite, Washington. Tectonophysics 398, 141-166,
625   doi: 10.1016/j.tecto.2005.02.001.

626 Friis-Christensen, E., Luhr, H., Hulot, G., 2006. Swarm: A constellation to study the Earth's
627   magnetic field. Earth Planets and Space 58, 351-358.

628 Guillong, M., Meier, D.L., Allan, M.M., Heinrich, C.A., Yardley, B.W.D., 2008. SILLS: A
629   MATLAB-based program for the reduction of laser ablation ICP-MS data of
630   homogeneous materials and inclusions. Miner. Assoc. Canada Short Course 40, 328-
631   333.

632 Haggerty, S.E., Baker, I., 1967. The alteration of olivine in basaltiv and associated lavas. Part
633   I: High temperature alteration. Contribution in Mineralogy and Petrology 16, 233-257.

634 Hoffmann, V.H., Hochleitner, R., Torii, M., Funaki, M., Mikouchi, T., Kaliwoda, M.,
635   Jenniskens, P., Shaddad, M.H., 2011. Magnetism and mineralogy of Almahata Sitta
636   polymict ureilite (= asteroid 2008 TC3): Implications for the ureilite parent body
637   magnetic field. Meteoritics and Planetary Science 46, 1551-1564, doi: 10.1111/j.1945-
638   5100.2011.01248.x.Hoye, G.S., O'Reilly, W., 1972. A magnetic study of the ferro-
639   magnesian olivines $(Fe_xMg_{1-x})SiO_4$, $0 < x < 1$. Journal of Physics and Chemistry of
640   Solids 33, 1827-1834.

641 Hrouda, F., 1982. Magnetic anisotropy of rocks and its application in geology and geophysics.
642   Geophysical Surveys 5, 37-82.

643 Hrouda, F., 2004. Problems in interpreting AMS parameters in diamagnetic rocks., in: Martín-
644   Hernández, F., Lüneburg, C.M., Aubourg, C., Jackson, M. (Eds.), Magnetic Fabric:
645   Methods and Applications. The Geological Society, London, UK, pp. 49-59.

646 Hrouda, F., Faryad, S.W., Jeřábek, P., Chlupáčová, M., Vitouš, P., 2009. Primary magnetic
647   fabric in an ultramafic body (Moldanubian Zone, European Variscides) survives
648   exhumation-related granulite-amphibolite facies metamorphism. Lithos 111, 95-111,
649   doi: 10.1016/j.lithos.2008.10.004.

650 Jarosewich, E., Nelen, J.A., Norberg, J.A., 1980. Reference samples for electron microprobe
651   analysis. Geostandards Newsletter 4, 43-47.

652 Jelinek, V., 1981. Characterization of the magnetic fabric of rocks. Tectonophysics 79, T63-
653   T67.

654 Jelinek, V., 1984. On a mixed quadratic invariant of the magnetic susceptibility tensor.
655   Journal of Geophysics 56, 58-60.

656   Kane, R.E., 2004. The creation of a magnificent suite of peridot jewelry: From the Himalayas
657   to Fifth Avenue. Gems & Gemology, 40, 288-302.

658   Kurat, G., Palme, H., Embey-Isztin, A., Touret, J., Ntaflos, T., Spettel, B., Brandstätter, F.,
659   Palme, C., Dreibus, G., Prinz, M., 1993. Petrology and geochemistry of peridotites and
660   associated vein rocks of Zabargad Island, Red Sea, Egypt. Mineralogy and Petrology
661   48, 309-341.

662   Lappe, S.-C., Church, N.S., Kasama, T., Bastos da Silva Fanta, A., Bromiley, G., Dunin-
663   Borkowski, R.E., Feinberg, J.M., Russell, S., Harrison, R.J., 2011. Mineral magnetism
664   of dusty olivine: A credible recorder of pre-accretionary remanence. Geochemistry
665   Geophysics Geosystems 12, Q12Z35, doi:10.1029/2011GC003811.

666   Laugier, J., Filhol, A., 1983. An interactive program for the interpretation and simulation of
667   Laue patterns. Journal of Applied Crystallography 16, 281-283.

668   Leroux, H., Libourel, G., Lemelle, L., Guyot, F., 2003. Experimental study and TEM
669   characterization of dusty olivines in chondrites: Evidence for formation by in situ
670   reduction. Meteoritics & Planetary Science 38, 81-94, doi: 10.1111/j.1945-
671   5100.2003.tb01047.x.

672   Martín-Hernández, F., Hirt, A.M., 2001. Separation of ferrimagnetic and paramagnetic
673   anisotropies using a high-field torsion magnetometer. Tectonophysics 337, 209-221,
674   doi: 10.1016/s0040-1951(01)00116-0.

675   Martín-Hernández, F., Hirt, A.M., 2004. A method for the separation of paramagnetic,
676   ferrimagnetic and haematite magnetic subfabrics using high-field torque
677   magnetometry. Geophysical Journal International 157, 117-127, doi: 10.1111/j.1365-
678   246X.2004.02225.x.

679   Müller, R., Fuess, H., Brown, P.J., 1982. Magnetic properties of synthetic fayalite (α-
680   Fe_2SiO_4). Le Journal de Physique Colloques 43, C7-249-C247-252.

681   Nagata, T., 1961. Rock magnetism, 2nd ed. Maruzen, C., Tokyo.

682   Nagata, T., Yukutake, T., Uyeda, S., 1957. On magnetic susceptibility of olivines. Journal of
683   Geomagnetism and Geoelectricity 9, 51-56.

684   Neumann, F.E., 1885. Vorlesungen über die Theorie der Elastizität der festen Körper und des
685   Lichtäthers, in: Meyer, O.E. (Ed.). B.G. Teubner Verlag, Leipzig, Germany.

686   Nicolas, A., Christensen, N.I., 1987. Formation of anisotropy in upper mantle peridotites: A
687   review, in: Fuchs, K., Froidevaux, C. (Eds.), Composition, Structure and Dynamics of
688   the Lithosphere-Asthenosphere System, Geodyn. Ser. AGU, Washington, D.C., pp.
689   111-123.

690   Owens, W.H., Bamford, D., 1976. Magnetic, seismic, and other anisotropic properties of rock
691   fabrics. Philosophical Transactions of the Royal Society A 283, 55-68.

692   Pettke, T., Oberli, F., Audetat, A., Guillong, M., Simon, A., Hanley, J., Klemm, L.M., 2012.
693   Recent developments in element concentration and isotope ratio analysis of individual
694   fluid inclusions by laser ablation single and multiple collector ICP–MS. Ore Geol.
695   Rev. 44, 10-38, doi: 10.1016/j.oregeorev.2011.11.001.

696   Rochette, P., Weiss, B.P., Gattacceca, J., 2009. Magnetism of extraterrestrial materials.
697   Elements 5, 223-228, doi: 10.2113/gselements.5.4.223.

698   Rudnick, R.L., Shan, G., Ling, W.L., Liu, Y.S., McDonough, W.F., 2004. Petrology and
699   geochemistry of spinel peridotite xenoliths from Hannuoba and Qixia, North China
700   craton. Lithos 77, 609-637, doi: 10.1016/j.lithos.2004.03.033.

701   Schmidt, V., Hirt, A.M., Rosselli, P., Martín-Hernández, F., 2007. Separation of diamagnetic
702   and paramagnetic anisotropy by high-field, low-temperature torque measurements.
703   Geophysical Journal International 168, 40-47, doi: 10.1111/j.1365-
704   246X.2006.03202.x.

705   Silver, P.G., 1996. Seismic anisotropy beneath the continents: Probing the depths of geology.
706   Annual Review of Earth and Planetary Sciences 24, 385-432.

707   Tommasi, A., Knoll, M., Vauchez, A., Signorelli, J.W., Thoraval, C., Logé, R., 2009.
708   Structural reactivation in plate tectonics controlled by olivine crystal anisotropy.
709   Nature Geoscience 2, 423-427, doi: 10.1038/ngeo528.

710   Uehara, M., Nakamura, N., 2006. Experimental constraints on magnetic stability of
711   chondrules and the paleomagnetic significance of dusty olivines. Earth and Planetary
712   Science Letters 250, 292-305, doi: 10.1016/j.epsl.2006.07.042.Xuexiang, Q.,
713   Grimmer, J.C., Zhiqin, X., 2009. Ultrahigh-pressure texture inheritance during
714   retrogression: Evidence from magnetofabrics in eclogites and ultramafic rocks
715   (Chinese Continental Scientific Drilling project). Tectonophysics 475, 267-278, doi:
716   10.1016/j.tecto.2008.09.015

717   Table 1: Sample locations, sample masses and forsterite and fayalite contents

718

719   Table 2: Saturation remanence and its effect on susceptibility

720

721   Table 3: Paramagnetic Curie temperatures and g-factors obtained from low-temperature
722   susceptibility curves of Ol14 and Ol15